Journal of Materials Chemistry A

ROYAL SOCIETY OF CHEMISTRY

PAPER

View Article Online
View Journal

Cite this: DOI: 10.1039/d6ta02595a

Engineering hierarchical porosity in MOFs for host–guest chemistry with large organometallic complexes

Jakob Blaschke, [a] Maria Asghar,[b] Zheao Huang, [a] Stephen Nagaraju Myakala, [a] Shaghayegh Naghdi, [a] Thomas Schachinger, [c] Hanspeter Kählig, [d] Olga Lanaridi, [e] Andreas Limbeck, [e] Jérôme Durand, [f] Philippe Serp, [fg] Florian Libisch, [b] Dogukan H. Apaydin *[a] and Dominik Eder *[a]

The microporous nature of metal–organic frameworks (MOFs) often limits their capacity to incorporate large molecular guests, such as organometallic catalysts. In this work, we demonstrate a defect-engineering strategy for the Zr-based MOF UiO-66 to generate hierarchical pore structures capable of hosting the bulky Lehn-type complex [Re(bpy-4-COOH)$(CO)_3$Cl]. By introducing missing-linker and missing-cluster defects-both during synthesis and through a selective ligand removal (SeLiRe) process-we modulate the framework's pore structure and volume. Using a post-synthetic modification approach, 2,2′-bipyridine-4-carboxylic acid (bpy-4-COOH) is anchored into the MOF structure *via* solvent-assisted ligand incorporation, followed by complexation with [$Re(CO)_5$Cl]. A comprehensive suite of characterization techniques including TGA, Ar-physisorption, STEM-EDX, solid-state NMR, XAS and other spectroscopic methods confirmed the formation and uniform distribution of the Re-complex within the MOF porosity. Our results show that the introduced defects and the associated creation of mesoporosity are essential for successful incorporation of the large Re-complex, while nearly defect-free UiO-66 cannot be modified with the ligand post-synthetically. The use of the SeLiRe process enables us to gain reasonable control over the amount of the Re-complex inside the MOF and leads to a homogeneous distribution throughout the particles. Photocatalytic CO_2RR experiments show CO as the main product with high selectivity when using TEOA as a sacrificial agent. This work demonstrates the potential of engineering hierarchical porosity in MOFs for immobilizing large, catalytically active molecular species in a stable and well-defined environment.

Received 26th March 2026
Accepted 2nd June 2026

DOI: 10.1039/d6ta02595a

rsc.li/materials-a

Introduction

MOFs have emerged over the past decade as highly tunable platforms for applications ranging from heterogeneous catalysis and water purification to gas storage and drug delivery[1–6] -an area of chemistry recognized by the 2025 Nobel Prize. These crystalline and often porous materials are built from an inorganic cluster or ion, connected with organic linkers. Their modular design enables the synthesis of isoreticular structures of a material – where the underlying secondary building unit (SBU) and topology remain constant while pore size and functionality are tuned by varying linker length or composition.[7] For example, the UiO-series (UiO-66, UiO-67 and UiO-68, UiO = Universitetet i Oslo) share the same inorganic $Zr_6O_4(OH)_4$ cluster and face-centered cubic topology, yet pore apertures span from 6 Å to 10 Å by increasing the number of phenyl rings from 1 to 3 in the dicarboxylate linker.[8–10] MOFs from the UiO-family have been widely employed as heterogeneous catalysts (either unmodified or after the introduction of defects and or metal-nanoparticles); however, these materials are not intrinsically active for photocatalysis and are typically modified with photoactive metal complexes to impart such functionality.[11–16] In this context, host–guest chemistry in MOFs describes the selective inclusion and organization of molecular 'guests' within a crystalline 'host' lattice, where pore size, aperture, and chemical functionality govern uptake, orientation, and

[a]Institute of Materials Chemistry, TU Wien, Getreidemarkt 9/BC/02, Vienna 1060, Austria. E-mail: dominik.eder@tuwien.ac.at; dogukan.apaydin@tuwien.ac.at
[b]Institute of Theoretical Physics, TU Wien, Wiedner Hauptstraße 8-10, 1040, Vienna, Austria
[c]University Service Centre for Transmission Electron Microscopy (USTEM), TU Wien, Wiedner Hauptstraße 8-10, Vienna 1060, Austria
[d]Department of Organic Chemistry, Faculty of Chemistry, University of Vienna, Währinger Str. 38, Vienna 1060, Austria
[e]Institute of Chemical Technologies and Analytics, TU Wien, Getreidemarkt 9, Vienna 1060, Austria
[f]Laboratoire de Chimie de Coordination, UPR CNRS 8241, Composante ENSIACET, Université de Toulouse, UPS-INP-LCC, 4 Allée Emile Monso, BP 44362, 31030 Toulouse Cedex 4, France
[g]Institut Universitaire de France (IUF), 1 Rue Descartes, Paris F-75231, France

dynamics. For bulky organometallic complexes, successful host–guest engagement hinges on matching framework architecture to guest dimensions and interaction motifs (*e.g.*, coordination or secondary interactions).

Molecular catalysts are celebrated for their superior selectivity and tunability, enabled by well-defined coordination environments. Their incorporation into porous frameworks creates hybrid materials that couple molecular control with accessible, structured pore networks. MOFs offer a promising bridge between homogeneous and heterogeneous catalysis by providing a stable, high-surface-area support that can preserve the unique activity of molecular catalysts while offering the benefits of a heterogeneous platform.[17–20] Anchoring such catalysts within MOFs combines the advantages of both catalytic paradigms: robust framework encapsulation with the fine control over reaction pathways typical of molecular species.[19–23] Additionally, this combination allows for the design of tailored environments for studying confinement effects of molecular complexes in porous supports.[24] Despite their high surface areas and structural robustness, conventional MOFs are inherently microporous (pore size < 2 nm), limiting the diffusion and encapsulation of bulky guest molecules.[25–28] Isoreticular expansion can lead to increased pore sizes and give the possibility of linker functionalization for direct incorporation of molecular complexes. Previous publications have functionalized UiO-67 with metal complexes by replacing part of the biphenyldicarboxylic acid linker with a bipyridine-dicarboxylic acid, which serves as a binding site for many catalytically active metal complexes.[14,25,29–32] However, the availability and cost of modified biphenyl linkers can be a hindrance for the synthesis of functionalized UiO-67 materials. Additionally, the increase in linker length has been shown to decrease the MOF stability in aqueous (especially acidic) or humid environments.[33] While UiO-66 doesn't share these disadvantages, the pores of the pristine framework are too small to host larger organometallic complexes.[25] A potential solution could be the selective ligand removal (SeLiRe) strategy, which has recently been developed to introduce controlled mesoporous structures *via* defect engineering.[34–39] During this process, a mixed-linker MOF is heated to a temperature at which one of the linkers is selectively removed due to differences in their thermal stability, leading to hierarchical pore systems. Feng *et al.* as well as Bueken *et al.* have shown that the process can be used to create mesoporous structures in UiO-66 by mixing either NH_2-BDC or *trans*-1,4-cyclohexane-dicarboxylate with BDC during the synthesis and later removing it *via* a thermal treatment.[36,39] In contrast to the random addition of defects during solvothermal synthesis, SeLiRe provides better control over cavity or pore-formation, which is essential for the incorporation of catalyst species and has been used previously for the functionalization of hierarchically porous MOFs with metal ions or metal nanoparticles.[40–42] Here, we utilise the previously established SeLiRe strategy and defect generation *via* synthetic parameters in UiO-66 to deliberately generate hierarchical micro-mesoporosity with coordinatively accessible defect sites, which in turn enables the post-synthetic SALI of bpy-4-COOH and in-pore formation of the bulky Lehn-type [Re(bpy-4-COO^-)$(CO)_3Cl$] complex. Under identical conditions, a nearly defect-free UiO-66 does not incorporate bpy-4-COOH, directly linking SeLiRe-derived hierarchical porosity and defect-anchoring sites to the successful uptake and uniform distribution of the Re-complex within the framework. Unlike prior UiO-67 linker-functionalization routes for incorporating Re complexes, which rely on modified biphenyl linkers,[29,31,32,43] or the addition of metal complexes during the synthesis,[15,16] this work applies SeLiRe in UiO-66 to enable the post-synthetic incorporation of the complex.

In this work, UiO-66 synthesis parameters were systematically tuned to modulate defect formation, enabling a versatile defect-control strategy in UiO-66 to generate hierarchical micro-mesoporous architectures capable of accommodating the Lehn-type complex [Re(bpy-4-COOH)$(CO)_3Cl$], a Re-complex with activity in the photocatalytic CO_2 reduction reaction (CO_2RR) to CO.[44] Our strategy leverages host–guest chemistry, wherein hierarchical meso-micro porosity and tailored binding sites in UiO-66 act in concert to admit, position, and retain this large organometallic guest. We employ both missing-linker (ML) and missing-cluster (MC) defect motifs-introduced synthetically and *via* SeLiRe-to modulate pore connectivity and size, creating large, interconnected pores that facilitate the transport of guest molecules through the MOF. Post-synthetic, solvent-assisted ligand incorporation (SALI) of 2,2′-bipyridine-4-carboxylic acid introduces the electron rich *N*,*N*-moiety on defect sites, which is followed by sequential metalation of a Re-precursor to generate the immobilized catalyst within the pore network (Scheme 1). We first characterize the defect distribution and porosity evolution in UiO-66 under varied synthesis conditions and then quantify bipyridine loading and Re incorporation by NMR, TGA, physisorption, LA-ICP-MS and STEM-EDX. Our results provide a proof-of-concept for engineering defects in MOFs *via* the established SeLiRe technique to host large molecular catalysts and set the stage for the design of next-generation hybrid catalytic materials.

Results

In total, four base samples were produced to study the effect of defect type and density on the incorporation of large metal–organic complexes into UiO-66. The first two samples, UiO and UiO_{NH_2}, have been synthesized *via* a microwave-assisted method following the protocol developed by Taddei *et al.*[45] The Zr-precursor ($ZrCl_4$) and a stoichiometric amount of organic linker with respect to Zr were dissolved in DMF and heated to 120 °C for 15 min (see SI for experimental details). In the case of UiO, only terephthalic acid (benzene-1,4-dicarboxylic acid, BDC) was utilized as the organic linker and in the case of UiO_{NH_2} a mixture of 90% BDC and 10% 2-amino-terephthalic acid (NH_2-BDC) were used to generate a mixed-linker MOF. The mixed-linker MOF was then subjected to a heat treatment at 310 °C for 12 h (see experimental details in the SI and Fig. S3) thereby selectively removing NH_2-BDC ligands. At this temperature, the bond between the NH_2-BDC ligands and the cluster is broken first on one side, followed by decarboxylation and after breaking the second connection to the cluster the remaining aniline

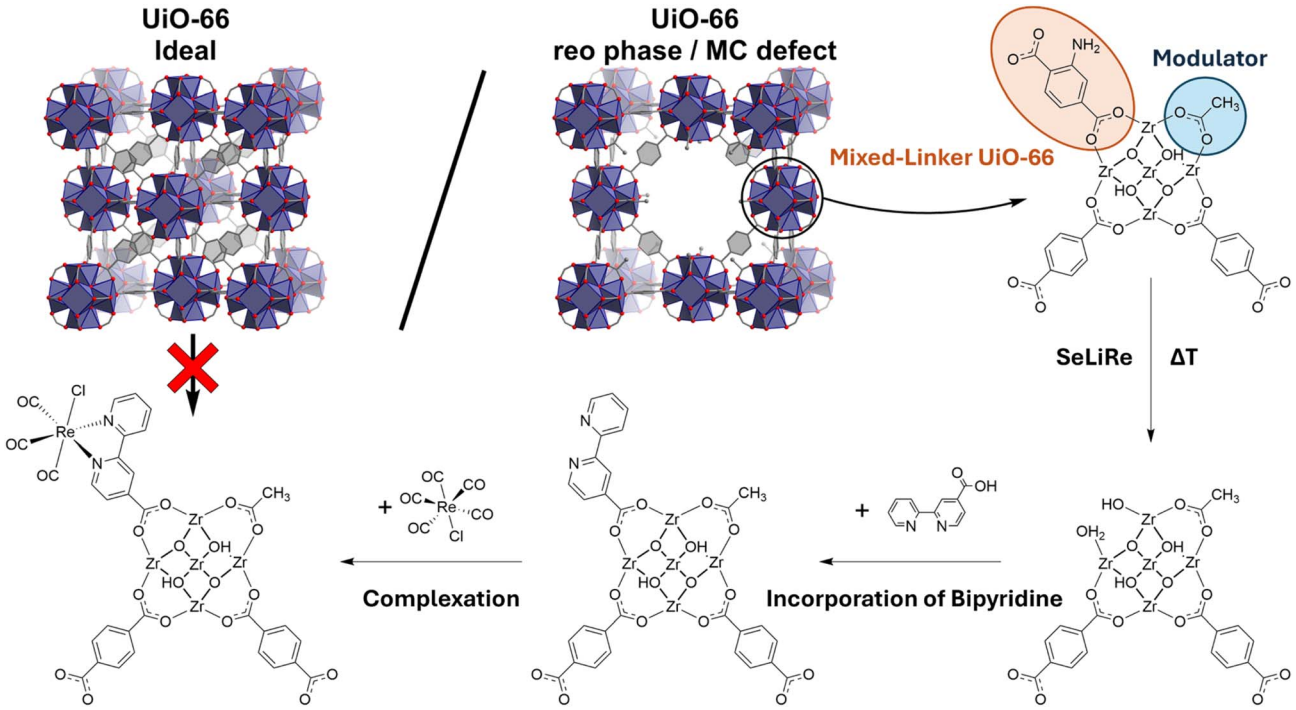

Scheme 1 Synthesis steps used to modify UiO-66 with the large molecular complex [Re(bpy-4-COO^-)$(CO)_3$Cl].

readily oxidizes creating open sites on the Zr-clusters in the process.[35,36] This sample with selectively removed ligands was designated UiO_{SeLiRe}. All samples contained a certain degree of random and uncontrolled ML and MC defects arising from the equimolar Zr : linker ratio in the synthesis, low reaction temperature and short reaction time. The further thermal treatment of UiO_{SeLiRe} enhanced the formation of ML defects by specifically removing the NH_2-BDC linkers and capping agents, which were still attached to the Zr-clusters. To provide a reference without ML defects, an "ideal" UiO-66 (nearly ML defect-free) was prepared following the procedure published by Shearer *et al.*[46] by heating a mixture of two equivalents of BDC with one equivalent of Zr-precursor at 220 °C for 24 h in an autoclave (see Experimental details in the SI). The use of a higher temperature, longer synthesis time and excess ligand led to a significantly reduced defect concentration in UiO_{Ideal}.

The synthesized powders showed particle sizes between 200–500 nm and while the samples synthesized by the microwave-assisted method had an octahedral shape, the particles of UiO_{Ideal} looked more rounded (see SEM images in Fig. S1). Powder XRD patterns (Fig. S2) of UiO and UiO_{NH_2} match the simulated UiO-66 pattern, with no extraneous peaks observed. UiO_{SeLiRe} also maintained all characteristic UiO-66 reflections matching the UiO_{NH_2}-sample in position and intensity, confirming that the addition of the second linker (NH_2-BDC) and the subsequent heat treatment do not alter the overall crystal structure. Additionally, no secondary phases (*e.g.*, ZrO_2) were observed. Defective UiO-66 often exhibits superlattice reflections between $2\theta = 4°$ and 6°, characteristic of correlated MC (reo) domains.[47,48] These superlattice reflections were not observed in Bragg–Brentano measurements (powder placed on a Si zero-background holder, Fig. S2). However, when the sample is measured in a capillary mode using an extended scan time of 12 h the superlattice reflections are readily observed (Fig. 1a). While UiO shows a single broad feature centered at ~5°, UiO_{Ideal} shows two sharp peaks at 4° and 6°. The reason for the difference has previously been attributed to different sized reo-regions in the MOF.[48] While regions of correlated MC defects produce the two distinct peaks at 4° and 6° (UiO_{Ideal}), smaller regions of isolated MC produce the broad peak (UiO).

^{1}H-NMR spectra of the dissolved MOFs (a.k.a digested) (Fig. 1b) revealed an intense peak at 7.8 ppm, assigned to BDC^{2-} in accordance with Shearer *et al.*[48] The additional peaks at 7.5, 7.1 and 7.0 ppm confirm the incorporation of NH_2-BDC^{2-} for the mixed-linker sample UiO_{NH_2} and verify the successful incorporation of the amino-linker in the framework (expected shifts were determined from dissolving only NH_2-BDC in the same solvent and analyzing the dissolved linker with the same measurement parameters). Relative quantification of the signals of BDC and NH_2-BDC yield a ratio of NH_2-BDC/total linkers of 11% which fits with the intended ratio of 10% (see Fig. S4). A resonance at 8.3 ppm is assigned to formate-generated by DMF decomposition during synthesis-which acts as a modulator by capping some of the Zr-cluster binding sites, generating ML defects.[48] After selective ligand removal, UiO_{SeLiRe} exhibits a complete disappearance of peaks corresponding to NH_2-BDC^{2-} and formate, while the BDC signal remains, confirming the selective and complete removal of the thermolabile linker NH_2-BDC (see Fig. S5). Notably, no new signals attributable to decomposition products are observed, contrasting with Feng *et al.*, where incomplete NH_2-BDC degradation produced 2-aminobenzoic acid residues.[36] The absence of such residues here suggests that

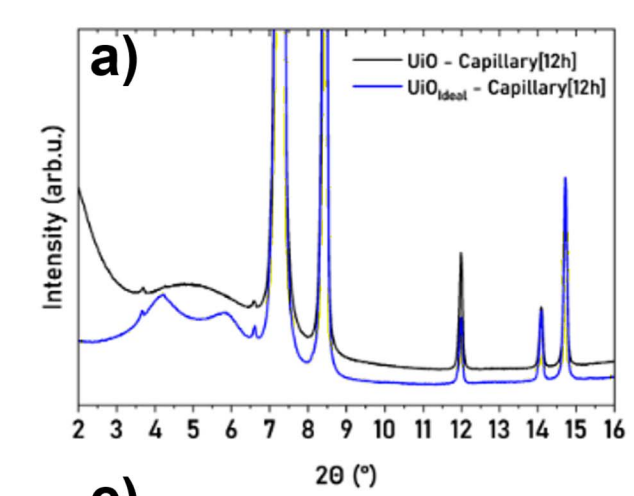

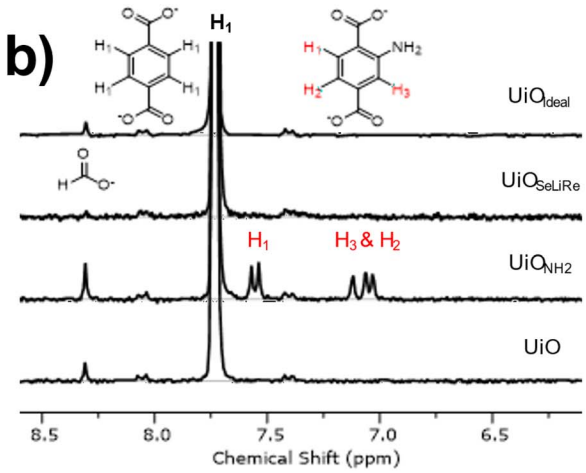

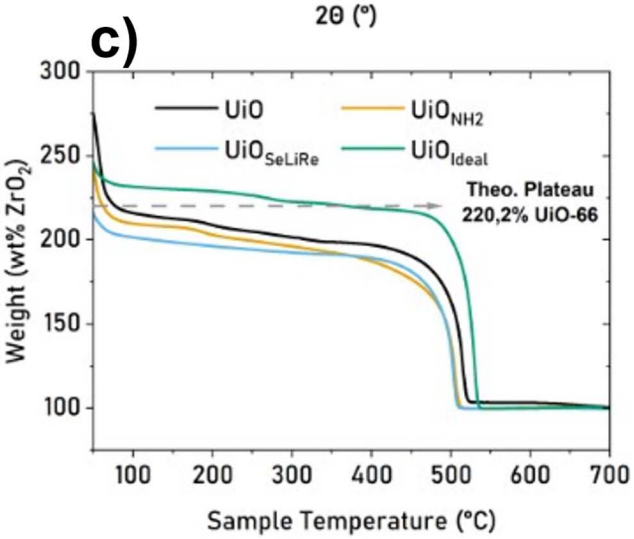

d)

Sample	TGA plateau [%ZrO_2]	# of linkers / Zr_6	#bpy-4-COOH / Zr_6	#Re / Zr_6
UiO	189 %	8.9	0.39	0.39
UiO_{NH2}	186 %	8.5	0.20	0.37
UiO_{SeLiRe}	180 %	8.0	0.46	0.43
UiO_{Ideal}	219%	11.8	0.00	-

Fig. 1 (a) Low-angle PXRD ($2\theta = 2$–$16°$) collected in capillary mode with an extended acquisition time (12 h) can resolve reo-type superlattice reflections arising from correlated missing-cluster (MC) domains. UiO exhibits a single broad feature centered at ~5°, indicative of smaller, isolated MC regions, whereas UiO_{Ideal} shows two sharp reflections at ~4° and ~6°, consistent with better-correlated reo domains despite the overall reduced ML defect concentration. (b) ^{1}H-digestion NMR spectra and (c) TGA curves under a constant flow of synthetic air of the 4 base samples. (d) Table showing the TGA-plateaus as well as the calculated connectivities, number of bipyridines per Zr_6-cluster from digestion NMR and the amount of Re per Zr_6-cluster calculated from LA-ICP-MS analysis.

the extended calcination time employed was sufficient to achieve complete removal.

TGA analysis was performed in air up to a temperature of 700 °C to track the different weight loss profiles and calculate an average linker connectivity of the Zr-clusters (Fig. 1c). The TGA curves of the UiO-type frameworks show several distinct weight loss steps which are in corroboration with previous studies.[36,48] According to these, the degradation profile can be described by the following steps: below 100 °C, desorption of physisorbed H_2O and residual solvents, adsorbed from the atmosphere. Between 100–400 °C, the TGA curve contains several overlapping weight loss steps corresponding to dehydroxylation of the inorganic clusters, loss of entrapped DMF and loss of formate and acetate modulator.[48] Finally, between 400–550 °C, the largest weight loss step comprises the loss of the BDC linkers and the collapse of the organic framework yielding ZrO_2. Additional characterization with *in situ* FTIR and NMR spectroscopy of the Ti-based MOF MIL-125 have revealed a 2-step decarboxylation process during the thermal degradation of MIL-125, which, due to the similar Lewis acidity of Ti^{4+} and Zr^{4+}, suggests a similar mechanism in UiO-66 based MOFs.[35] While the TGA curves of UiO and UiO_{Ideal} are well described by these steps, UiO_{NH_2} exhibits a continuous mass loss between 300 and 350 °C, most likely due to the removal of thermolabile NH_2-BDC linkers. In this case, this linker weight loss overlaps with the loss of monocarboxylate ligands as well as the loss of BDC linkers at higher temperatures. In the case of UiO_{SeLiRe}, the TGA curve shows no distinct weight loss step between 100–400 °C since the heat treatment has already removed all the thermolabile NH_2-BDC as well as formate ligands and remaining DMF. The remaining weight loss could be explained by a gradual dehydroxylation of the clusters as well as removal of trapped organic fragments remaining in the pores. This is also supported by the digestion NMR spectra (see Fig. 1b), which show no detectable NH_2-BDC or formate ligands remaining in the MOF after the heat treatment process.

Since the magnitude of the final weight loss step depends on the amount of BDC linkers present in the MOF, it is possible to calculate the average number of linkers per Zr-cluster from the mass loss due to BDC-combustion.[10,46,48–50] A fully dehydroxylated, defect-free UiO-66 would exhibit a plateau at 220.2 wt%, which corresponds to a dehydroxylated composition of $Zr_6O_6(\text{-BDC})_6$ (see the section "Determination of MOF composition" in the SI). UiO_{Ideal} shows a plateau very close to this value (see Fig. 1c, dashed arrow) indicating an almost complete 12-linker coordination. In contrast, UiO, UiO_{NH_2} and UiO_{SeLiRe} reach lower plateau values due to ML defects[48] from which the SBU connectivity (linkers per cluster) can be calculated. Fig. 1d shows the average connectivity for each sample yielding 11.8 for UiO_{Ideal} and reduced connectivities of 8.9, 8.5 and 8.0 for UiO, UiO_{NH_2} and UiO_{SeLiRe}, respectively.

Consistent with prior reports that key synthesis parameters (temperature, time, and ligand/modulator stoichiometry) strongly influence UiO-66 cluster connectivity,[46] the conditions used here for UiO and UiO_{NH_2} (120 °C, 15 min, and an equimolar Zr : BDC ratio) produce highly defective materials, reflected in the reduced average connectivities (~8.5–8.9) relative to the ideal 12. Interestingly, while the mixed-linker sample UiO_{NH_2} exhibited a close match between the intended and observed linker ratio, it still showed a substantial amount of ML defects, indicating that deficiencies in both BDC and NH_2-BDC contribute to the defect structure. In contrast, the UiO_{Ideal} sample prepared under optimized conditions approaches the defect-free limit (11.8), in line with the trends established by Shearer *et al.* and in spite of the MC defects observed in the capillary PXRD measurements.[46] The SeLiRe treatment reduced the average number of linkers per Zr_6 cluster in UiO_{SeLiRe} even further (8.0).

To evaluate the porosity of the base samples, Ar isotherms were recorded at 87 K (Fig. 2a) since the use of Ar is usually preferred for the evaluation of pores smaller than 2 nm.[51] To compare the evaluation with the more typical N_2 physisorption, additional isotherms were recorded at 77 K using N_2 gas (see Fig. S6 and S7), and the results were comparable in both cases. All samples are highly porous, and exhibit Brunauer–Emmett–Teller (BET) surface areas higher than 1000 $m^2\ g^{-1}$ (see Table S1). The isotherm of UiO_{SeLiRe} displays a small hysteresis loop at intermediate relative pressure (~0.4–0.9 p/p_0). Its shape is H2-type,[51] consistent with constricted mesopores, expected from mesopore formation *via* SeLiRe. The UiO and UiO_{NH_2} curves are nearly overlapping, showing only a very subtle hysteresis, suggesting minor H4-like features, *i.e.*, microporous frameworks with limited mesoporosity.[51] UiO_{Ideal} shows no visible hysteresis, typical of a purely microporous material, consistent with a nearly defect-free UiO-66. The corresponding density functional theory (NLDFT) pore distributions in Fig. 2c show that all the samples have a large number of micropores centered at *ca.* 6 Å. UiO, UiO_{NH_2} and UiO_{SeLiRe} also exhibit an additional, smaller peak centered at *ca.* 15 Å, indicating a second type of larger micropore, attributable to localized MC defects.[36,47] These findings align with the appearance of the "broad" low-angle peak in the PXRD diffractograms of UiO (see Fig. 1a), associated with reo-type defect domains.[48] Interestingly, UiO_{Ideal} does not exhibit a peak at 15 Å, despite PXRD evidence for MC defects. One plausible explanation is that MC defects are present but partially 'filled' by non-bridging BDC linkers coordinated to a single Zr cluster and oriented into the vacant pore, effectively suppressing the appearance of a larger-pore feature in the adsorption-derived distribution. An alternative explanation would be occluded, unreacted BDC molecules within the pores; however, combined TGA and digestion NMR point to minimal linker deficiency in UiO_{Ideal}, making this less likely. After the heat treatment and selective ligand removal, UiO_{SeLiRe} retains the 6 Å peak but develops mesoporosity in the 20–80 Å range, attributable to the loss of the NH_2-BDC ligand and concomitant pore enlargement. Correspondingly, the height and area of the peak at 15 Å decrease relative to UiO_{NH_2} consistent with a fraction of these larger micropores coalescing into mesopores. This behavior has already been observed and described for UiO-66 and the Ti-based MOF MIL-125 (see also Fig. 5a and b).[35,36]

Modification with bpy-4-COOH

Following characterization, the pristine materials were subjected to post-synthetic modification with 2,2′-bipyridine-4-carboxylic acid (bpy-4-COOH) anchoring the bipyridine for subsequent formation of the Re-complex in the next step. The MOFs UiO, UiO_{NH_2}, UiO_{SeLiRe}, and UiO_{Ideal} were stirred with bpy-4-COOH in DMF overnight (see Experimental section in the SI) to incorporate the new ligand *via* SALI. The newly formed samples were designated UiO-bpy, UiO_{NH_2}-bpy, UiO_{SeLiRe}-bpy and UiO_{Ideal}-bpy. To quantify the amount of bpy-4-COOH, digestion NMR experiments were performed after thorough washing of the samples with fresh DMF and methanol. Fig. 3a shows the successful incorporation of bpy-4-COOH in UiO, UiO_{NH_2} as well as UiO_{SeLiRe}. In contrast, UiO_{Ideal}-bpy contains no detectable bpy-4-COOH signal under identical conditions, suggesting that defect sites and/or larger pores are essential for incorporating bulky ligands. The absence of larger pores and free binding sites in UiO_{Ideal} likely prevents uptake of the bipyridine. By combining the relative integration of bpy-4-COOH to the linker peaks and the independently determined number of linkers per cluster, we calculate the amount of bpy-4-COOH per cluster for each sample (Fig. 1d and Table S2). UiO_{SeLiRe} exhibits the highest loading-nearly twice that of UiO_{NH_2}-consistent with its hierarchical porosity and greater abundance of accessible defect sites that facilitate diffusion and binding. Collectively, these results underscore the critical role of defect density and pore architecture in enabling the incorporation of bulky ligands into UiO-66-type frameworks.

To further elucidate how the bipyridine is incorporated into the framework, solid-state ^{13}C-NMR analyses were performed. Fig. 3b shows the spectra of UiO_{SeLiRe} before and after the reaction with bpy-4-COOH, a physical mixture between bpy-4-COOH and UiO_{SeLiRe} (UiO_{SeLiRe} + bpy) and the spectrum of pure bpy-4-COOH. The 3 large peaks at 170, 135, and 127 ppm in UiO_{SeLiRe}, UiO_{SeLiRe}-bpy and UiO_{SeLiRe} + bpy belong to the terephthalate linkers inside the framework. Additionally, the spectrum of UiO_{SeLiRe}-bpy shows several peaks which were assigned to the bipyridine inside the

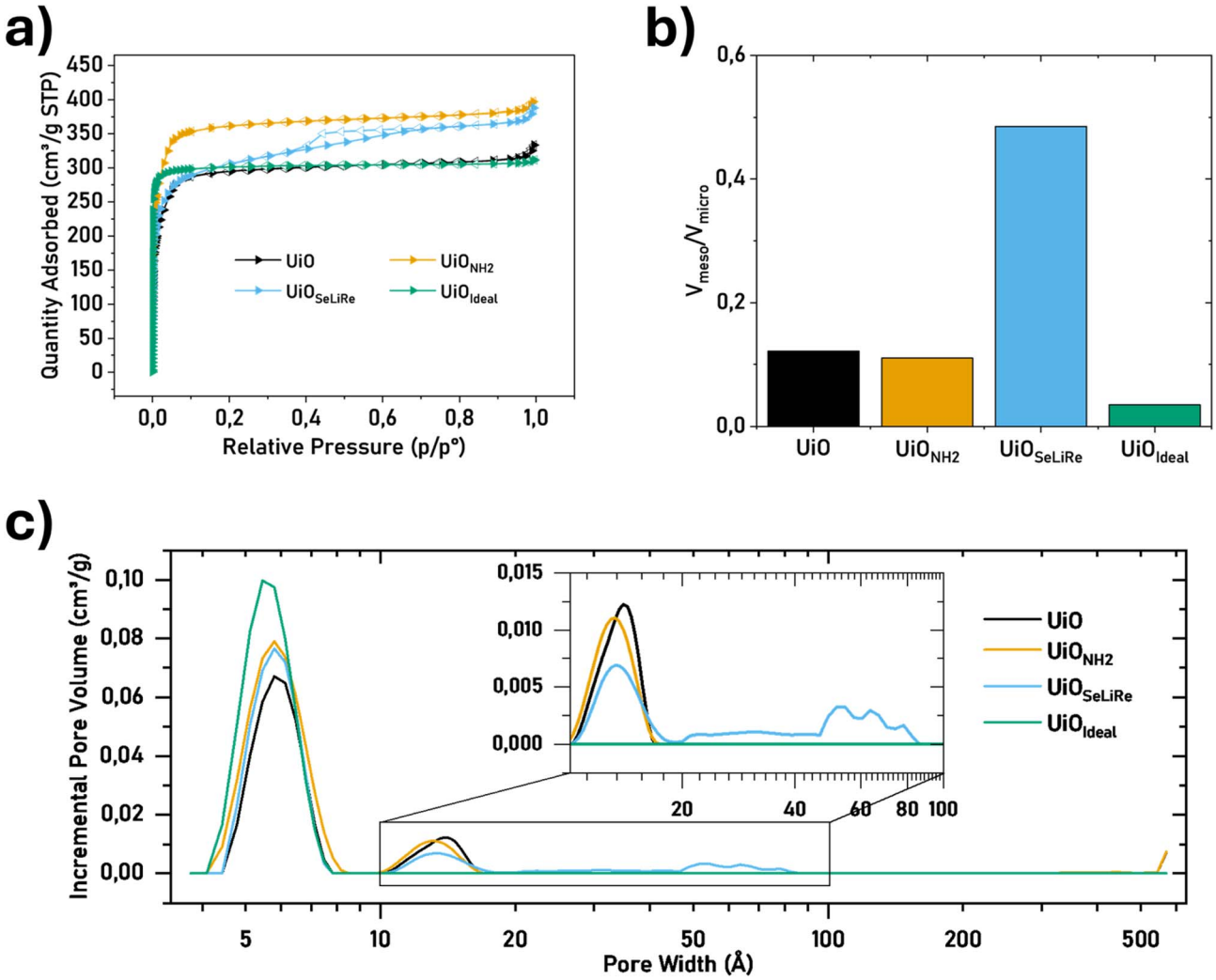

Fig. 2 Ar physisorption results: (a) Ar isotherms measured at 87 K. (b) ratios of total mesopore volume (V_{meso}) to total micropore volume (V_{micro}). (c) NLDFT pore distribution of the 4 base samples before modification. The results show a large increase in mesoporosity for UiO$_{SeLiRe}$ and evidence of MC defects in the defective samples UiO, UiO$_{NH_2}$ and UiO$_{SeLiRe}$.

framework (157, 149, and 123 ppm). The pristine linker, bpy-4-COOH, exhibits a low intensity peak at 174 ppm, assigned to the quaternary carbon from the free carboxylic acid group. After MOF modification, this peak disappears, consistent with coordination of the carboxylic acid to the MOF-clusters forming a carboxylate and with the removal of non-coordinated species during washing. However, intense peak of the terephthalate carboxylates at 170 ppm, has a broad base that extends further than 174 ppm, potentially masking any signal from residual free carboxylic acid. Still, the increase in chemical shift by 2–3 ppm in UiO$_{SeLiRe}$-bpy *versus* UiO$_{SeLiRe}$ + bpy indicates some interaction with the positively charged Zr-cluster and is thus consistent with the incorporation of the ligand into the pores of the framework.[52,53]

Complex formation of [Re(bpy-4-COO$^-$)(CO)$_3$Cl]

Following the modification of the MOF-materials with bpy-4-COOH, they were further reacted with [Re(CO)$_5$Cl] to form the targeted [Re(bpy-4-COO$^-$)(CO)$_3$Cl] complex in the pores. The resulting materials-UiO-Re, UiO$_{NH_2}$-Re & UiO$_{SeLiRe}$-Re – were characterized using PXRD (see Fig. S8) and N_2-physisorption (see Fig. S9). The three modified samples still showed all expected peaks in the PXRD diffractogram for UiO-66 and no additional peaks from a potential [Re(bpy-4-COOH)(CO)$_3$Cl] phase. Furthermore, the samples are still highly porous, exhibiting a slight reduction in their surface area to about 800 $m^2\ g^{-1}$ and a lower pore volume, consistent with the modification of the pores. During the reaction, the samples underwent a visible color change to yellow, which was further studied by UV-vis diffuse reflectance spectroscopy (DRS, Fig. 4a). While the pure [Re(bpy-4-COOH)(CO)$_3$Cl] complex in solution shows an absorption band centered at 367 nm, which corresponds to the metal-to-ligand charge transfer (MLCT) band of this complex,[54] the Re-modified MOFs all show red-shifted bands centered around 393 nm, 412 nm, and 394 nm for UiO-Re, UiO$_{NH_2}$-Re, and UiO$_{SeLiRe}$-Re respectively. This indicates electronic coupling

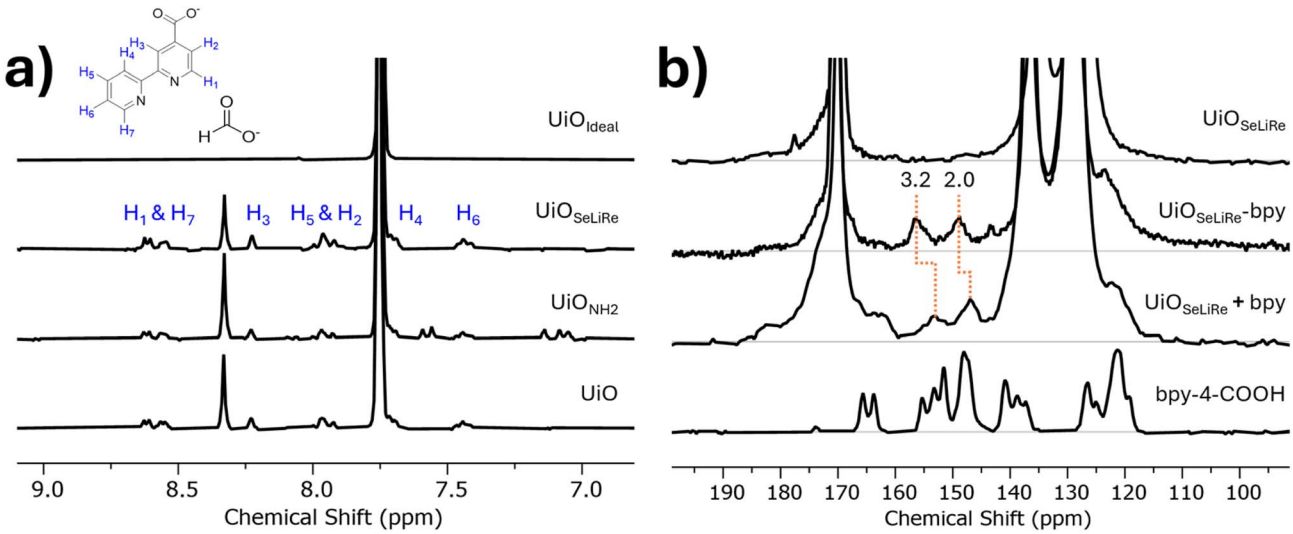

Fig. 3 (a) ^{1}H-NMR digestion NMR showing new peaks belonging to bpy-4-COOH for every sample except for UiO$_{Ideal}$. (b) ^{13}C-solid-state NMR spectra of UiO$_{SeLiRe}$, UiO$_{SeLiRe}$-bpy, UiO$_{SeLiRe}$ + bpy (a physical mixture between the MOF and bpy) and the pure bpy-4-COOH showing a shift in the bpy-4-COOH signals upon incorporation into the MOF pores.

between the carboxylate-bound Re complex and the UiO-66 framework.[16,54,55] The latter two samples already show absorption in this region before the modification (see Fig. S10a). Accordingly, the new peak is only visible as a shoulder on the peak at 351 nm in the case of UiO$_{NH_2}$ and the center position was calculated by fitting the shape with Gauss peaks (see Fig. S10). Su *et al.* have also observed a shift in the MLCT band of the same complex with a dicarboxylated bipyridine incorporated into UiO-66; however, in the opposite direction (blue-shift), which was attributed to luminescence rigidochromism.[16] This is likely due to the rigorous spatial confinement of the Lehn-type catalyst in their UiO-66 samples, hindering the free rotation of the complex. In contrast, the added porosity in our samples provides more rotational freedom for the Re-complex, *i.e.*, the electronic interactions dominate over the steric effects. Furthermore, the complex synthesized by Su *et al.* has an additional free carboxylic acid group, which could further hinder the movement of the complex in the pores.[16] The bathochromic shift of the MLCT band upon immobilization indicates a modified local electronic environment for the Re center within UiO-66. DFT calculations reproduce the direction and magnitude of the shift and suggest a redistribution of charge density from the Zr node toward the bipyridine ligand upon binding, accompanied by increases in the HOMO and LUMO energies relative to the free complex (see Computational analysis of optical and charge properties of Re-modified UiO-66). These results are consistent with host–guest interactions at defect-bound sites modulating the frontier levels of the immobilized complex.

To further characterize the electronic properties of the newly formed material, photoluminescence (PL) emission spectra of UiO and UiO-Re were compared with a physical mixture of UiO

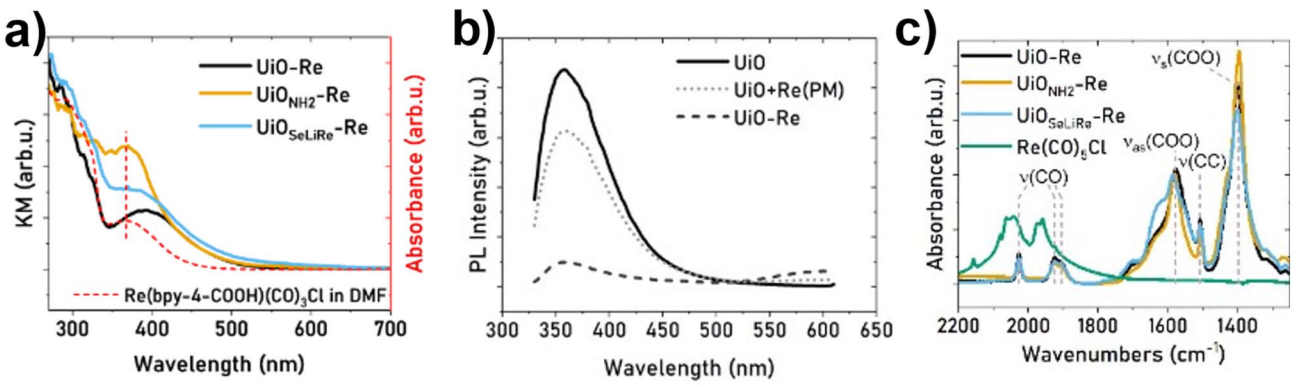

Fig. 4 (a) DRS spectra of the Re-modified samples. The three samples show a new peak which was assigned to the MLCT of the Re-complex inside the pores. It is shifted compared to the homogeneous complex in solution, indicating a confined environment in the pores. (b) PL emission spectra (excitation 310 nm) of UiO, UiO-Re and a physical mixture between UiO and [Re(bpy-4-COOH)(CO)$_3$Cl] showing decreased luminescence for UiO-Re indicative of charge transfer between the MOF and the complex. (c) ATR-FTIR spectra of the Re-modified samples, showing three new bands, which are characteristic for the formation of the [Re(bpy-4-COO$^-$)(CO)$_3$Cl] complex.

and the pure complex [Re(bpy-4-COOH)$(CO)_3$Cl] (UiO + Re, see Fig. 4b for UiO and Fig. S12 for UiO_{NH_2} and UiO_{SeLiRe}). All samples exhibited luminescence; however, the PL intensity of the Re-modified samples was significantly reduced compared to the unmodified ones, hinting at a photoinduced electron transfer process from the photoexcited MOF to the confined Re-complex. The physical mixture also displayed a decrease in PL intensity, albeit to a lesser extent, effectively ruling out secondary absorption of emitted light by the Re-complex as the primary cause for the quenching.

The successful anchoring of the complex was further confirmed using ATR-FTIR spectroscopy (Fig. 4c). All materials show three characteristic peaks of the MOF backbone at 1583, 1507, and 1395 cm^{-1}, which were assigned to the asymmetric stretching of carboxylate (COO^-), aromatic C=C stretching and symmetric carboxylate stretching from the terephthalate linkers, respectively. The shift and splitting pattern of the ν(CO) bands (2026, 1925, 1910 cm^{-1}) relative to [Re$(CO)_5$Cl] is characteristic of a facial tricarbonyl Re(I) center bound to bipyridine, consistent with [Re(bpy-4-COO^-)$(CO)_3$Cl] indicating a change in the coordination environment and successful complexation within the MOF.

To quantify the Re loading, LA-ICP-MS measurements were performed on UiO-Re, UiO_{NH_2}-Re and UiO_{SeLiRe}-Re (Fig. 1d as well as Table S2), yielding Re/Zr molar ratios from which the number of Re-atoms per Zr_6-cluster was calculated. This elemental quantification technique offers significant advantages for samples that are difficult to dissolve or where only a limited amount of sample is available.[56] Because of differences in absorbed moisture content and the limited sample amount, exact weighing was not possible, therefore, only the relative Re/Zr ratio was considered. For UiO-Re and UiO_{SeLiRe}-Re, the Re-loading closely matches the bpy-4-COO^- loadings per Zr_6-cluster, indicating that all the bipyridine moieties have formed the Re-carbonyl complex. However, in UiO_{NH_2}-Re the amount of Re is approximately twice as large as the number of bpy-4-COO^- groups (see Fig. 1d). This could be attributed to an additional stabilization of Re *via* the NH_2-groups of the second linker (NH_2-BDC).

TEM images of UiO-Re and UiO_{SeLiRe}-Re (Fig. 5a and b) showed homogeneous particles of approx. 200 nm in size. While the particles of UiO-Re show some differences in brightness due to overlapping areas, the particles of UiO_{SeLiRe}-Re show small bright spots which could be indicative of mesopores in the sample which decrease the density of the particle.[36] Elemental mapping *via* STEM-EDX of UiO_{SeLiRe}-Re (Fig. 5d–g) revealed a curved shape of the lateral Re-distribution (Fig. 5h), which importantly follows the distribution of Zr as well. Fig. 5i shows a schematic representation of the expected STEM-EDX profiles resulting from different Re-distributions in the MOF particle for the observed orientation of the particle. The measured profile aligns more closely with a model in which Re is evenly distributed throughout the MOF pores. This aligns with the previous results that report the Re-complex resides predominantly within the pores rather than being anchored on the external surface. The homogeneous Re distribution across entire crystallites corroborates the spectroscopic interpretations by excluding phase segregation or surface agglomeration as origins of the observed optical changes.

To gain deeper structural insights into the local coordination environment of the anchored Re centers, synchrotron X-ray absorption spectroscopy (XAS) measurements were conducted in fluorescence mode with a solid-state detector to ensure high-quality data acquisition despite the heavy Zr-matrix. X-ray absorption near-edge structure (XANES) spectra for both UiO_{NH_2}-Re and UiO_{SeLiRe}-Re exhibit nearly identical edge positions located between that of Re foil (Re(0)) and ReO_2 (Re(IV)), consistent with a Re(I) oxidation state (Fig. 6a and S12 as well as additional XPS spectra of UiO_{SeLiRe}-Re in Fig. S15).[57] Furthermore, the spectra display a sharp and intense white line peak characteristic of molecular Re-carbonyl complexes, arising from the 2p → 5d transition into discrete unoccupied molecular orbitals.

Extended X-ray absorption fine structure (EXAFS) analysis and Wavelet Transform (WT) plots revealed distinct differences in the coordination spheres of the two samples (Fig. 6b–e and S13 and S14). To better assess the local coordination environments, the EXAFS data were refined by freely floating the coordination numbers (only constraint applied was to the Debye–Waller factors, σ^2). For UiO_{SeLiRe}-Re, the freely coordination numbers for Re–C (2.8), Re–N (2.4), and Re–Cl (0.8) are in great agreement with the theoretical values of the [Re(bpy-4-COO^-)$(CO)_3$Cl] (Table S3). This confirms the successful and pristine complexation of the target structure within the engineered MOF.

In contrast, the unconstrained *R*-space analysis of UiO_{NH_2}-Re indicates a distinct coordination environment. Notably, the fit yielded a significantly elevated average Re–C coordination number of 3.9. This increase in carbonyl coordination serves as evidence for a mixed-species system within the framework. It corroborates the LA-ICP-MS results, indicating that alongside the bpy-coordinated complex, a substantial fraction of the Re precursor may coordinate with the free amino groups ($-NH_2$) of the BDC linkers. In this secondary interaction, the Re center likely retains four carbonyl ligands, forming a [Re(NH_2-MOF)$(CO)_4$Cl] species.

Computational analysis of optical and charge properties of Re-modified UiO-66

To analyze the optical properties and charge distributions of the synthesized complexes further, DFT calculations were performed to compare the Re-complex attached in the MOF with an isolated [Re(bpy)$(CO)_3$Cl] complex solvated in DMF (see Fig. S11). To describe the isolated complex solvated in DMF, we employed an implicit solvation method. To account for solvation effects, *i.e.*, the electrostatic environment created by the solute, several approaches are available, including the polarizable continuum model (PCM), the conductor like screening model (COSMO), or the self-consistent continuum solvation (SCCS) model.[58–60] For this study, we used an "Multipole Expansion (MPE) implicit solvation method" that combines accuracy with computational efficiency.[61] It effectively partitions the whole system into subdomains coupled

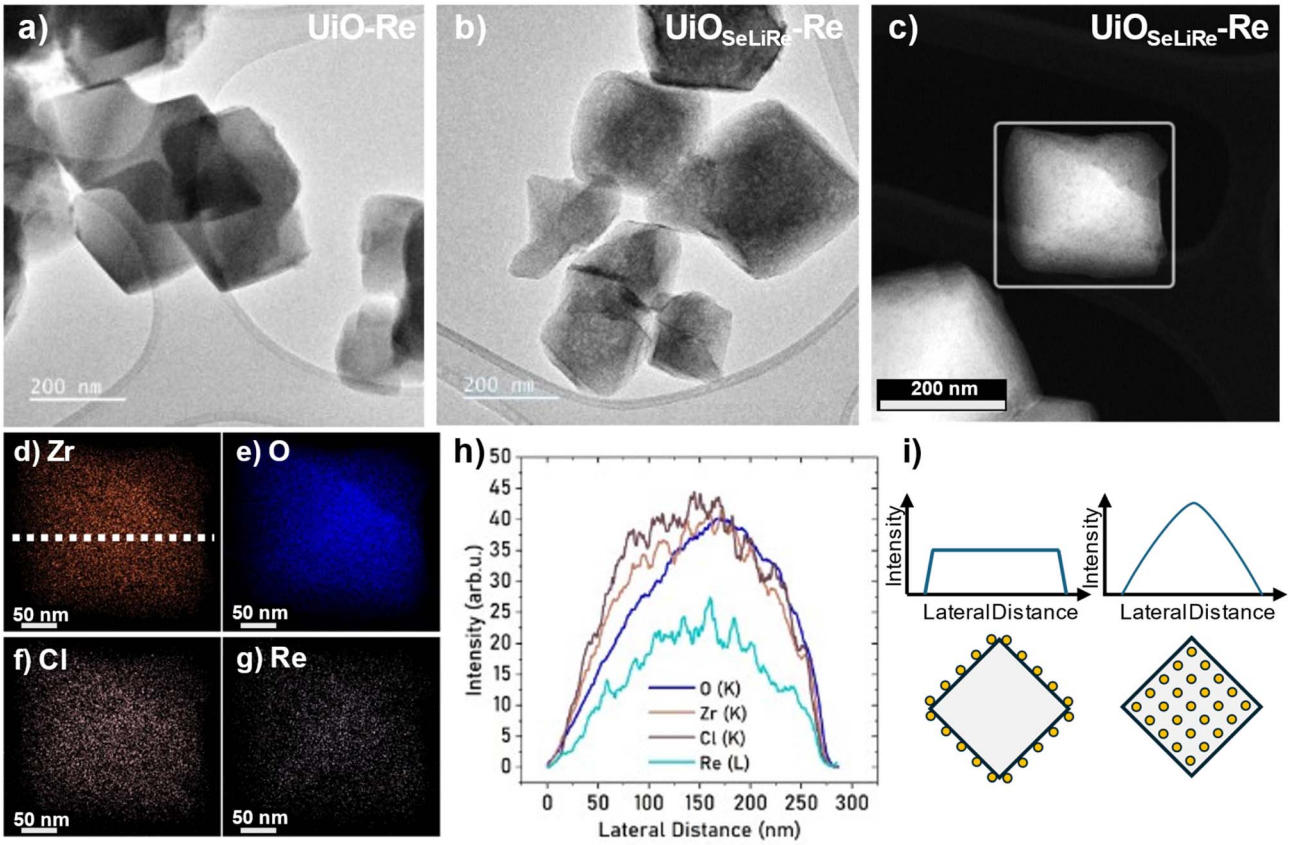

Fig. 5 (a) TEM image of UiO-Re and (b) UiO$_{SeLiRe}$-Re showing bright areas in the particle which could indicate the formation of mesopores. (c) STEM image of UiO$_{SeLiRe}$-Re with the STEM-EDX elemental mapping for zirconium, oxygen, chlorine and rhenium shown in (d–g). (h) is an extracted line profile along the line drawn in (d) from the mappings in (d–g) showing the lateral homogenous distribution of several elements across the particle displayed in the STEM image. (i) Expected STEM-EDX scan profiles resulting from pure surface attachment and a homogenous distribution of a species throughout the particle.

via an electrostatic boundary condition and solves multiple coupled Poisson equations at different dielectric permittivities. We used the dielectric constant of DMF ($\varepsilon_r = 36.7$) as solvent permittivity.[62]

Modeling the Re-complex embedded within UiO-66 is more challenging, considering the possibility of (partial) presence of DMF remaining from the synthesis. To obtain a tractable system size, we replaced the full organic linkers (terephthalic acid) of the $Zr_6O_4(OH)_4$ cage with hydrogens, while retaining all the details of the charge transfer between UiO-66 and the [Re(bpy-4-COO$^-$)(CO)$_3$Cl] complex. This gave us a cluster with preserved local coordination geometry at the attachment site with a substantially lower number of atoms and hence lower number of basic functions. Compared to the full 228-atom supercell of UiO-66, such a simple cluster allows an easy systematic analysis of electronic couplings between the $Zr_6O_4(OH)_4$ cage and the Re-complex, including direct insight into the charge transfer between them. We investigated two relative orientations of the Re-complex with respect to the cage, differentiated by the dihedral angle of rotation (α) at the point of attachment. α is defined as the angle between the Re-complex's molecular plane and the plane created by the carboxylate attachment group. Upon relaxation we found two local minima with $\alpha_1 = 55.0°$ (Orientation-1) and $\alpha_2 = -6.2°$ (nearly coplanar, Orientation-2). To obtain an accurate description of the dielectric environment of the Re-complex embedded within the MOF, we used three different boundary conditions for both orientations: (i) periodic boundary conditions in a moderate-sized box, (ii) non-periodic cluster calculations in vacuum and (iii) the cluster embedded using an implicit solvation model (computational details for all these approaches are listed in the SI). For each boundary condition we calculated the total energy, Fermi energy and frontier orbital gap (HOMO–LUMO (H–L) gap) and compared them to the experimental values. The non-periodic and non-solvated cluster calculations (ii) yielded the closest agreement with the experiment. For simplicity, we focus here on this geometry exclusively, while the remaining results are discussed in the SI. The structural details of Orientation-1 are given in Fig. 7a while Orientation-2 is depicted in Fig. S16.

To elucidate the red shift observed in the experiment we performed an orbital analysis, which yields the energies of the HOMO and LUMO orbitals, and the H–L gap. The values are listed in Table 1 and iso-surface plots (Fig. 7b–e) show the dispersion of the charge cloud on the Re-complex before and after binding with the cage. Including further ligands, further delocalizes the LUMO along the carbon π-system of the ligands,

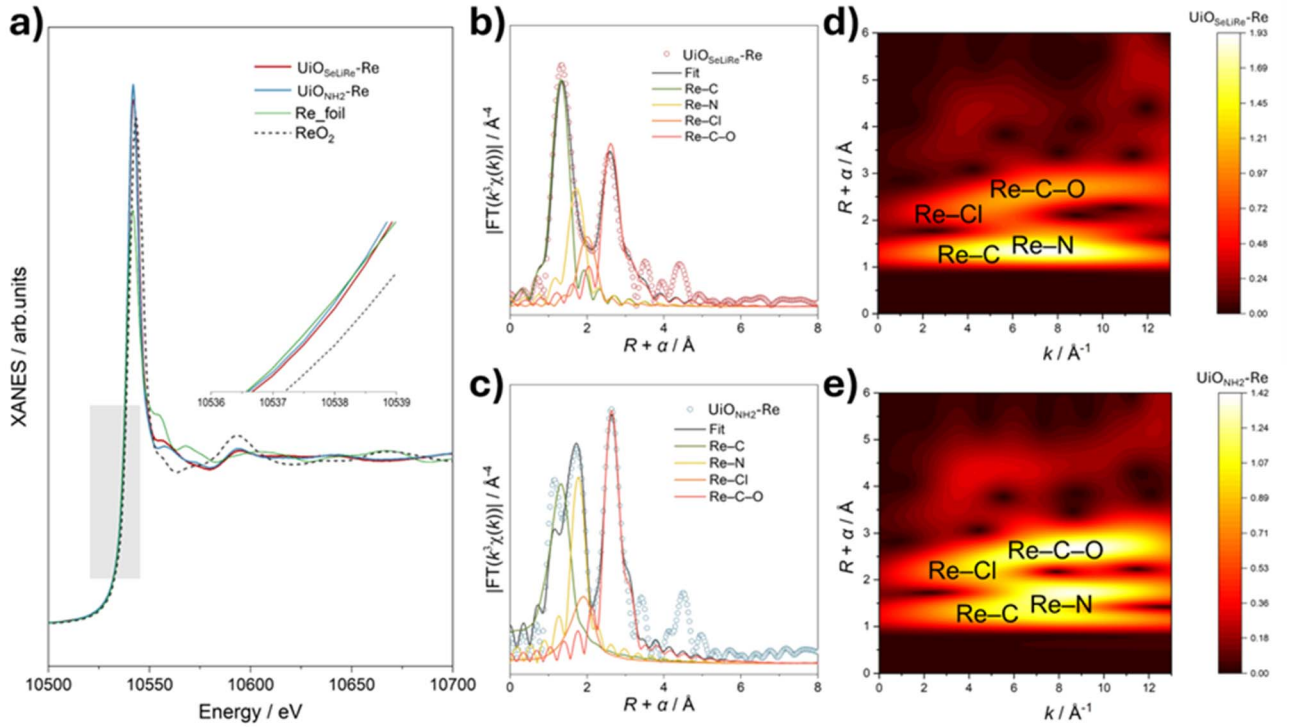

Fig. 6 (a) Re L_3-edge XANES spectra of UiO_{NH_2}-Re and UiO_{SeLiRe}-Re. Reference spectra for Re foil and ReO_2 are provided for comparison. (b and c) FT-EXAFS k^3-weighted $\chi(k)$ function spectra in R-space of UiO_{NH_2}-Re and UiO_{SeLiRe}-Re. (d and e) WT contour plots of UiO_{NH_2}-Re and UiO_{SeLiRe}-Re.

slightly reducing its energy (10 meV, see Fig. S17 & Table S4). The reduced H–L gaps after the complexation confirm the charge transfer between the Re-complex and cage, consistent with experimental observations. Linear-response time-dependent DFT calculations of the Re-complex confirm the lowest-energy peak in photoluminescence centred at the HOMO–LUMO gap (see Fig. S18), validating its role in estimating the influence of the MOF. The H–L gap changes from 3.37 eV (367.13 nm) for the solvated complex to 3.04 eV (407.81 nm) for the cage–bound complex, explaining the red shift observed in the experiment. The reduction in H–L gap is dominated by the lowering of the HOMO orbital in Orientation-1. By contrast, the LUMO orbital does not change much upon complexation. The lowering of the HOMO orbital energy explains the increase in charge transfer between the Re-complex and the MOF. The slight mismatch between the experimental values and the calculated value for Orientation-1 is probably due to the replacement of the linkers with hydrogen or remaining DMF inside the pores of the MOF. The slight increase in LUMO energy upon complex formation is consistent with the greater redistribution of electron density in the LUMO, which extends onto the Re complex, whereas the HOMO shows minimal change in its electronic distribution (see Fig. 7d–e and S19).

Mulliken charge analysis revealed the distribution of electron density before and after the attachment of the Re-complex to the Zr-cluster. Most of the atoms on Re-complex undergo small changes (~0.005 to 0.01). The charge density became more negative on the oxygen atom of the carbonyl group, indicating an accumulation of electron density upon complexation of the Re complex with MOF. The Re metal also showed a slight increase in electron density; however, the bipyridine-carbon attached to the carboxylate (see C15 in Fig. S20) becomes more positive showing a decrease in the electron density at this point. For a detailed list of notable changes in the Mulliken charge analysis, see Tables S78 and S9 in the SI.

Photocatalytic CO_2RR

To demonstrate the feasibility of using the synthesized materials for photocatalytic CO_2 reduction, experiments were conducted in DMF using triethanolamine (TEOA) as sacrificial agent under 365 nm irradiation in a sealed batch reactor at 15 °C (see SI for details). After 1 hour of illumination, gaseous products were quantified by GC and the results are displayed in Fig. 8a.

The pristine samples UiO and UiO_{Ideal} show no measurable evolution of CO or H_2, consistent with their negligible absorption at 365 nm (see Fig. S10). In contrast, both UiO_{NH_2} and UiO_{SeLiRe} produce small amounts of CO with minimal H_2, in line with their DRS absorption at 365 nm (Fig. S10) and prior reports of photocatalytic activity in NH_2-UiO-66.[63]

All Re-modified samples evolve mostly CO with a small amount of H_2. The CO rates increase in the order of UiO-Re < UiO_{NH_2}-Re < UiO_{SeLiRe}-Re (0.02, 0.11 & 0.14 μmol mg^{-1} h^{-1}). Although the Re-loadings of these samples are similar, the

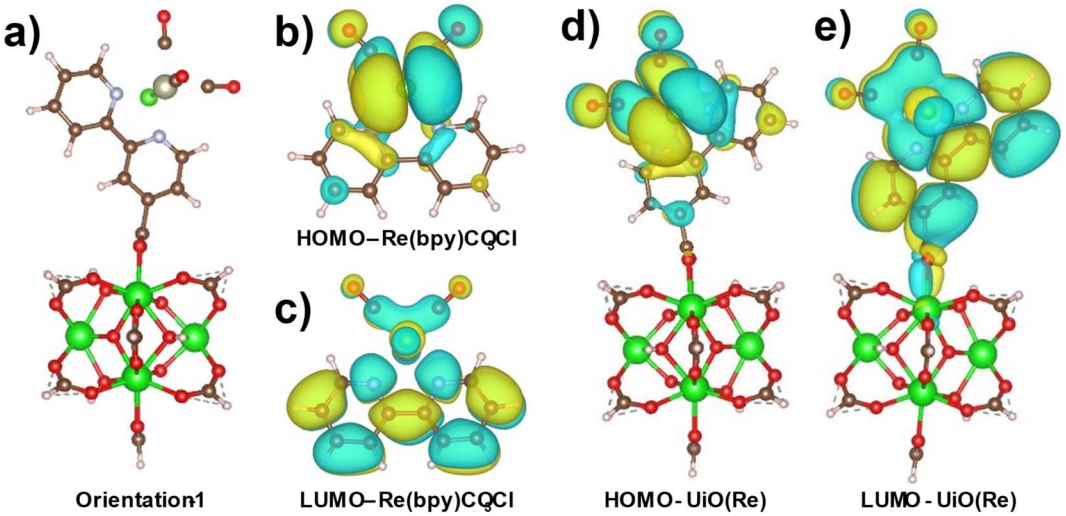

Fig. 7 (a) Relaxed geometry of Orientation-1 ($\alpha_1 = 55.0°$). The other images represent the isodensity plots (at 0.003) of the (b) HOMO orbital and (c) LUMO orbital of the Re-complex before attachment to the Zr-cluster as well as the (d) HOMO orbital and (e) LUMO orbital of the Re-complex after attachment to the Zr-cluster. Yellow and blue iso-surface parts correspond to two different signs of the wavefunction at the same density value. Atom colors represent Zr (large green spheres), Cl (small green sphere), O (red), C (black), N (light blue), Re (grey) and H (white).

increase in CO production of UiO_{SeLiRe}-Re is consistent with facilitated mass transport enabled by the hierarchical meso-microporosity, while UiO_{NH_2}-Re incorporates basic amino-groups which are reported to enhance affinity toward adsorption of CO_2 in the framework and enhance CO_2 activation.[63] This interpretation aligns with the MLCT red-shift, PL quenching, and homogeneous Re dispersion discussed above, which together indicate effective host–guest electronic coupling and intrapore catalysis.

To verify that CO_2 is the carbon source for the evolved CO (rather than adventitious carbon from the MOF or solvent), we performed control experiments by: (i) replacing CO_2 with Ar, (ii) stirring the reaction in the dark, and (iii) using only DMF without TEOA as a sacrificial agent (see Fig. S21). Under Ar, only trace CO and increased H2 were observed, indicating that CO_2 is required for elevated CO production. The dark and DMF-only controls yielded negligible product formation.

Catalyst recyclability and leaching were evaluated by filtering UiOSeLiRe-Re after reaction, redispersing the solid in fresh solvent, and repeating the experiment under identical conditions (1 h illumination). As shown in Fig. 8b, the recycled catalyst retains a large fraction of its initial activity, while the corresponding supernatant generates only trace amounts of CO, indicating a negligible homogeneous contribution from leached Re species. To quantify leaching, ICP-OES analysis of the post-reaction supernatant revealed that 16% of the total Re loading was present in solution after 1 h, confirming that the majority of Re remains confined within the MOF (see Fig. S22). After prolonged operation (21 h illumination), the dissolved Re fraction increased to 26%, suggesting that leaching occurs predominantly at early stages and that the framework remains largely stable under photocatalytic conditions.

As a homogeneous reference, dissolved [Re(bpy-4-COOH)$(CO)_3$Cl] was tested under the same conditions and the and the Re-normalized activity (turnover frequency, TOF) is depicted in Fig. 8c. The UiO_{SeLiRe}-Re material performs similarly to the molecular complex, with TOFs of 1.2 and 1.5 h^{-1} during the first hour of illumination, respectively. Both systems exhibit a marked loss of activity within the first 3 h, as evidenced by the long-term data in Fig. 8d. After that time, both catalysts only show a slight increase in their total turnover number (TON) during the next 19 h. Given that post-catalysis PXRD (Fig. S23) indicates the MOF framework remains intact, the observed activity loss may stem from deactivation of the Re-complex.[64]

Overall, these results demonstrate that defect engineering and hierarchical porosity in UiO-66 are crucial for incorporating and activating the Lehn-type Re complex, yielding selective CO_2-to-CO conversion with suppressed H_2 evolution and clear performance gains as pore accessibility and defect-bound binding sites increase.

Table 1 The HOMO and LUMO orbital energies of Re-complex before and after the attachment to the MOF, wavelengths from λ (nm) = 1240/E (eV). The UV-vis spectrum of the Re-complex in DMF can be seen in Fig. S11

Sample	HOMO (eV)	LUMO (eV)	Gap (eV)	Gap (nm)	Experimental values
Re-complex (in solvent)	−6.34	−2.96	3.38	367	370 nm
Orient.1 (no solvent)	−5.98	−2.94	3.04	408	393 nm

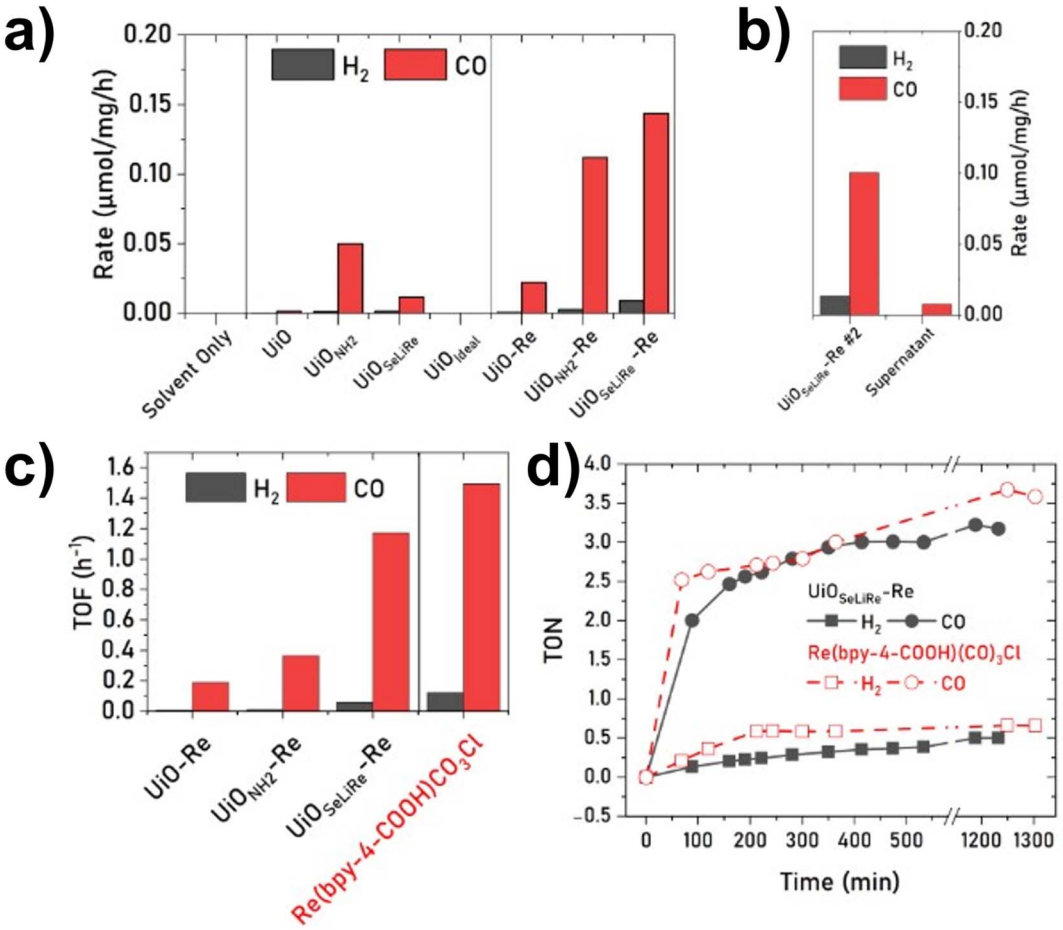

Fig. 8 Photocatalytic CO_2RR in DMF with TEOA under UV-LED illumination (365 nm): CO and H_2 production rates. (a) Unmodified samples show negligible or small amounts of CO, whereas Re-modified MOFs exhibit markedly higher CO rates with minimal H_2. (b) Repeating the CO_2RR experiment with the filtered UiO_{SeLiRe}-Re sample retains some of the original activity and the supernatant shows almost no activity (normalized to the same mass). (c) By normalizing the activity to the Re-amount, the results can be compared to the homogeneously dissolved [Re(bpy-4-COO^-)$(CO)_3$Cl]. (d) A long-term experiment of UiO_{SeLiRe}-Re and [Re(bpy-4-COO^-)$(CO)_3$Cl] shows a rapid decrease in activity over the first few hours, while still retaining a small base activity over the experiment duration of 21 h.

Conclusions

In this study we have demonstrated the successful immobilization of the bulky molecular catalyst [Re(bpy-4-COO^-)$(CO)_3$Cl] within the pores of UiO-66. Compared to prior UiO-67 strategies that rely on pre-functionalized biphenyl linkers or co-encapsulation approaches for Re-complex functionalization, our work introduces a UiO-66 platform in which hierarchical micro-mesoporosity and coordinatively accessible defect sites are generated *via* SeLiRe to enable post-synthetic admission and uniform immobilization of the bulky Lehn-type [Re(bpy-4-COO^-)$(CO)_3$Cl] complex. This lowers the cost and prevents stability drawbacks associated with modified biphenyl linkers in UiO-67, while providing more control over pore architecture and defect-anchoring sites that directly govern ligand uptake and loading in UiO-66, which is not achievable in nearly defect-free UiO-66. Beyond the uptake of the complex, we demonstrate MOF-complex electronic coupling (bathochromic MLCT shift and PL quenching), evidencing a modified local electronic environment for the immobilized Re-center.

Our results show that structural defects, specifically ML defects, play a critical role in enabling the incorporation of large molecular species. While the nearly defect-free UiO_{Ideal} was unable to accommodate the bipyridine ligand, all three defect-rich samples successfully incorporated bpy-4-COOH *via* SALI. Subsequent complexation with $[Re(CO)_5Cl]$ led to the formation of the target complex [Re(bpy-4-COO^-)$(CO)_3$Cl] within the MOF pores.

Among the defect-engineered samples, UiO_{SeLiRe}, which was derived from UiO_{NH_2} by selective ligand removal of amino-functionalized linkers, exhibited the highest bpy-4-COOH and Re loadings. Although UiO and UiO_{NH_2} contained random ML and MC defects from the synthesis, which permitted the incorporation of some Re-complex, these samples lacked the control over defect number and location achieved in the SeLiRe-modified sample. The introduced mesoporosity facilitates better dispersion of the complex in the MOF, thereby directly

controlling the incorporation of the Re-complex. Characterization by PXRD, digestion and solid-state NMR, physisorption, FTIR, PL, LA-ICP-MS and STEM-EDX confirmed the structural integrity of the materials and homogeneous incorporation of [Re(bpy-4-COO^-)$(CO)_3$Cl]. EXAFS confirmed the local coordination environment of the embedded complex, hinting at a difference in the specific coordination of Re in UiO_{SeLiRe}-Re and UiO_{NH_2}-Re due to the presence of an additional nitrogen binding site from the free $-NH_2$ groups. The pronounced PL quenching observed in UiO-Re further supports photoinduced electron transfer from the excited MOF to the Re-complex. Photocatalytic CO_2RR experiments show measurable CO evolution, confirming that the complex operates within the MOF pores, however, the composite deactivates quite rapidly, with only a fraction of the original activity remaining after 3 h.

Overall, this work demonstrates a proof-of-concept that hierarchical porosity and defect engineering in MOFs can be strategically employed to incorporate and stabilize large organometallic complexes, thereby expanding the functional landscape for catalysis and related applications.

Ulrich Schubert tribute

This article is dedicated to Prof. Ulrich Schubert on the occasion of his 80th birthday, honoring his outstanding ability to inspire scientists in the field of materials chemistry through excellent research and teaching.

Author contributions

Jakob Blaschke: conceptualization, data curation, formal analysis, investigation, methodology, visualization, writing – original draft, writing – review & editing. Maria Ashgar: formal analysis, methodology, visualization, writing – original draft. Zheao Huang: data curation, formal analysis, visualization, writing – original draft. Stephen Nagaraju Myakala: investigation. Shaghayegh Nagdhi: investigation, writing – original draft. Thomas Schachinger: investigation. Hanspeter Kählig: investigation. Olga Lanaridi: investigation. Andreas Limbeck: resources, supervision. Jérôme Durand: conceptualization, supervision. Philippe Serp: conceptualization, resources, supervision. Florian Libisch: resources, supervision. Dogukan H. Apaydin: conceptualization, funding acquisition, methodology, project administration, supervision, writing – review & editing. Dominik Eder: conceptualization, funding acquisition, methodology, project administration, resources, supervision, writing – review & editing.

Conflicts of interest

There are no conflicts to declare.

Data availability

Original data for generation of the figures is available under https://doi.org/10.48436/kprpn-bds10.

Supplementary information (SI): experimental details about synthesis and characterizations as well as theoretical and defect calculations, SEM, TGA, digestion NMR, N_2-physisorption data as well as DRS fitting, PL emission spectra and XAS data of additional samples and XPS spectra as well as additional theoretical calculations and reference CO_2RR experiments. See DOI: https://doi.org/10.1039/d6ta02595a.

Acknowledgements

Jakob Blaschke is recipient of a DOC Fellowship of the Austrian Academy of Sciences at the Institute of Materials Chemistry, TU Wien. This research was funded in part by the Austrian Science Fund (FWF) [10.55776/COE5] (Cluster of Excellence MECS). The authors thank Dr. Cornelia von Baeckmann for valuable discussions and input, especially regarding the interpretation of ssNMR results. The authors acknowledge the use of Chat-GPT for reviewing the manuscript for improved clarity and grammar. The authors acknowledge TU Wien Bibliothek for financial support through its Open Access Funding Programme.

References

1 S. Soni, P. K. Bajpai and C. Arora, A review on metal-organic framework: synthesis, properties and application, *Charact. Appl. Nanomater.*, 2020, **3**(2), 87–106, DOI: 10.24294/can.v3i2.551.
2 A. Bavykina, N. Kolobov, I. S. Khan, J. A. Bau, A. Ramirez and J. Gascon, Metal–Organic Frameworks in Heterogeneous Catalysis: Recent Progress, New Trends, and Future Perspectives, *Chem. Rev.*, 2020, **120**(16), 8468–8535, DOI: 10.1021/acs.chemrev.9b00685.
3 S. Rojas and P. Horcajada, Metal–Organic Frameworks for the Removal of Emerging Organic Contaminants in Water, *Chem. Rev.*, 2020, **120**(16), 8378–8415, DOI: 10.1021/acs.chemrev.9b00797.
4 H. D. Lawson, S. P. Walton and C. Chan, Metal–Organic Frameworks for Drug Delivery: A Design Perspective, *ACS Appl. Mater. Interfaces*, 2021, **13**(6), 7004–7020, DOI: 10.1021/acsami.1c01089.
5 S. Kitagawa, R. Kitaura and N. S. ichiro, Functional Porous Coordination Polymers, *Angew. Chem., Int. Ed.*, 2004, **43**(18), 2334–2375, DOI: 10.1002/anie.200300610.
6 H. Furukawa, K. E. Cordova, M. O'Keeffe and O. M. Yaghi, The Chemistry and Applications of Metal-Organic Frameworks, *Science*, 2013, **341**(6149), 1230444, DOI: 10.1126/science.1230444.
7 O. M. Yaghi, M. O'Keeffe, N. W. Ockwig, H. K. Chae, M. Eddaoudi and J. Kim, Reticular synthesis and the design of new materials, *Nature*, 2003, **423**(6941), 6941, DOI: 10.1038/nature01650.
8 J. H. Cavka, S. Jakobsen, U. Olsbye, *et al.*, A New Zirconium Inorganic Building Brick Forming Metal Organic Frameworks with Exceptional Stability, *J. Am. Chem. Soc.*, 2008, **130**(42), 13850–13851, DOI: 10.1021/ja8057953.
9 J. Winarta, B. Shan, S. M. Mcintyre, *et al.*, A Decade of UiO-66 Research: A Historic Review of Dynamic Structure, Synthesis

Mechanisms, and Characterization Techniques of an Archetypal Metal–Organic Framework, *Cryst. Growth Des.*, 2020, **20**(2), 1347–1362, DOI: 10.1021/acs.cgd.9b00955.

10 L. Valenzano, B. Civalleri, S. Chavan, *et al.*, Disclosing the Complex Structure of UiO-66 Metal Organic Framework: A Synergic Combination of Experiment and Theory, *Chem. Mater.*, 2011, **23**(7), 1700–1718, DOI: 10.1021/cm1022882.

11 A. Dhakshinamoorthy, A. Santiago-Portillo, A. M. Asiri and H. Garcia, Engineering UiO-66 Metal Organic Framework for Heterogeneous Catalysis, *ChemCatChem*, 2019, **11**(3), 899–923, DOI: 10.1002/cctc.201801452.

12 M. B. Chambers, X. Wang, N. Elgrishi, *et al.*, Photocatalytic Carbon Dioxide Reduction with Rhodium-based Catalysts in Solution and Heterogenized within Metal–Organic Frameworks, *ChemSusChem*, 2015, **8**(4), 603–608, DOI: 10.1002/cssc.201403345.

13 M. Liu, Y. F. Mu, S. Yao, *et al.*, Photosensitizing single-site metal−organic framework enabling visible-light-driven CO2 reduction for syngas production, *Appl. Catal., B*, 2019, **245**, 496–501, DOI: 10.1016/j.apcatb.2019.01.014.

14 X. H. Chen, Q. Wei, J. D. Hong, R. Xu and T. H. Zhou, Bifunctional metal–organic frameworks toward photocatalytic CO2 reduction by post-synthetic ligand exchange, *Rare Met.*, 2019, **38**(5), 413–419, DOI: 10.1007/s12598-019-01259-6.

15 Z. Su, B. Yu, J. Feng, M. Zhong, X. Li and J. Shi, Co-Encapsulation of Rhenium and Ruthenium Complexes into the Scaffolds of Metal–Organic Framework to Promote CO2 Reduction, *Catalysts*, 2023, **13**(12), 1510, DOI: 10.3390/catal13121510.

16 Z. Su, Y. Luo, J. Shi, *et al.*, Manipulating the Reaction Pathway of CO2 Photoreduction via the Microenvironment of a Re Molecular Catalyst, *J. Phys. Chem. Lett.*, 2023, **14**(13), 3208–3215, DOI: 10.1021/acs.jpclett.3c00459.

17 R. Reji, J. P. Vizuet, X. Yan, *et al.*, Photochemical CO2 Reduction by a Postsynthetically Modified Zr-MOF, *Inorg. Chem.*, 2025, **64**(36), 18304–18315, DOI: 10.1021/acs.inorgchem.5c02600.

18 S. Li, X. Shangguan, Z. Zhou, *et al.*, Immobilization of ferrocene and its derivatives within metal–organic frameworks with high loadings toward efficient oxygen evolution reaction, *Dalton Trans.*, 2024, **53**(4), 1568–1574, DOI: 10.1039/D3DT02763E.

19 S. R. V. Parambil, S. Karmakar, F. A. Rahimi and T. K. Maji, Confining Molecular Photosensitizer and Catalyst in MOF toward Artificial Photosynthesis: Validating Electron Transfer by In Situ DRIFT Study, *ACS Appl. Mater. Interfaces*, 2023, **15**(23), 27821–27831, DOI: 10.1021/acsami.3c01153.

20 S. Karmakar, S. Barman, F. A. Rahimi and T. K. Maji, Covalent grafting of molecular photosensitizer and catalyst on MOF-808: effect of pore confinement toward visible light-driven CO2 reduction in water, *Energy Environ. Sci.*, 2021, **14**(4), 2429–2440, DOI: 10.1039/D0EE03643A.

21 P. M. Stanley, J. Haimerl, N. B. Shustova, R. A. Fischer and J. Warnan, Merging molecular catalysts and metal–organic frameworks for photocatalytic fuel production, *Nat. Chem.*, 2022, **14**(12), 1342–1356, DOI: 10.1038/s41557-022-01093-x.

22 W. G. Sikorski, M. J. Mekkering, A. van der Weijden, S. Tanase, J. N. H. Reek and J. I. van der Vlugt, Photo-Driven CO2 Reduction With a Heterogenized Re Catalyst in the Metal–Organic Framework PCN-777: Effects of Catalyst Loading and Anchoring Strategy on Catalysis, *ChemSusChem*, 2026, **19**(2), e202502216, DOI: 10.1002/cssc.202502216.

23 P. M. Stanley, C. Thomas, E. Thyrhaug, *et al.*, Entrapped Molecular Photocatalyst and Photosensitizer in Metal–Organic Framework Nanoreactors for Enhanced Solar CO2 Reduction, *ACS Catal.*, 2021, **11**(2), 871–882, DOI: 10.1021/acscatal.0c04673.

24 M. Gouygou, P. Serp and J. Durand, Confinement Effects in Catalysis with Molecular Complexes Immobilized into Porous Materials. in *Catalysis in Confined Frameworks*. 2024, pp. 273–314, DOI: 10.1002/9783527839278.ch8.

25 P. M. Stanley, J. Haimerl, C. Thomas, *et al.*, Host–Guest Interactions in a Metal–Organic Framework Isoreticular Series for Molecular Photocatalytic CO2 Reduction, *Angew. Chem., Int. Ed.*, 2021, **60**(33), 17854–17860, DOI: 10.1002/anie.202102729.

26 M. H. Sun, S. Z. Huang, L. H. Chen, *et al.*, Applications of hierarchically structured porous materials from energy storage and conversion, catalysis, photocatalysis, adsorption, separation, and sensing to biomedicine, *Chem. Soc. Rev.*, 2016, **45**(12), 3479–3563, DOI: 10.1039/C6CS00135A.

27 G. Cai, P. Yan, L. Zhang, H. C. Zhou and H. L. Jiang, Metal–Organic Framework-Based Hierarchically Porous Materials: Synthesis and Applications, *Chem. Rev.*, 2021, **121**(20), 12278–12326, DOI: 10.1021/acs.chemrev.1c00243.

28 L. Feng, K. Y. Wang, X. L. Lv, T. H. Yan and H. C. Zhou, Hierarchically porous metal–organic frameworks: synthetic strategies and applications, *Natl. Sci. Rev.*, 2020, **7**(11), 1743–1758, DOI: 10.1093/nsr/nwz170.

29 C. Wang, Z. Xie, K. E. deKrafft and W. Lin, Doping Metal–Organic Frameworks for Water Oxidation, Carbon Dioxide Reduction, and Organic Photocatalysis, *J. Am. Chem. Soc.*, 2011, **133**(34), 13445–13454, DOI: 10.1021/ja203564w.

30 K. Ling, M. M. Ogle, E. Flores, F. Godoy and A. A. Martí, Exploring the Photophysical Properties of UiO-67 MOF Doped with Rhenium Carbonyl Complexes, *J. Photochem. Photobiol., C*, 2022, **11**, 100127, DOI: 10.1016/j.jpap.2022.100127.

31 K. M. Choi, D. Kim, B. Rungtaweevoranit, *et al.*, Plasmon-Enhanced Photocatalytic CO2 Conversion within Metal–Organic Frameworks under Visible Light, *J. Am. Chem. Soc.*, 2017, **139**(1), 356–362, DOI: 10.1021/jacs.6b11027.

32 X. Gao, B. Guo, C. Guo, Q. Meng, J. Liang and J. Liu, Zirconium-Based Metal–Organic Framework for Efficient Photocatalytic Reduction of CO2 to CO: The Influence of Doped Metal Ions, *ACS Appl. Mater. Interfaces*, 2020, **12**(21), 24059–24065, DOI: 10.1021/acsami.0c05631.

33 J. B. DeCoste, G. W. Peterson, H. Jasuja, T. G. Glover, Y. gui Huang and K. S. Walton, Stability and degradation

mechanisms of metal–organic frameworks containing the Zr6O4(OH)4 secondary building unit, *J. Mater. Chem. A*, 2013, **1**(18), 5642–5650, DOI: 10.1039/C3TA10662D.

34 S. M. Chavan, G. C. Shearer, S. Svelle, *et al.*, Synthesis and Characterization of Amine-Functionalized Mixed-Ligand Metal–Organic Frameworks of UiO-66 Topology, *Inorg. Chem.*, 2014, **53**(18), 9509–9515, DOI: 10.1021/ic500607a.

35 S. Naghdi, A. Cherevan, A. Giesriegl, *et al.*, Selective ligand removal to improve accessibility of active sites in hierarchical MOFs for heterogeneous photocatalysis, *Nat. Commun.*, 2022, **13**(1), 1, DOI: 10.1038/s41467-021-27775-7.

36 L. Feng, S. Yuan, L. L. Zhang, *et al.*, Creating Hierarchical Pores by Controlled Linker Thermolysis in Multivariate Metal–Organic Frameworks, *J. Am. Chem. Soc.*, 2018, **140**(6), 2363–2372, DOI: 10.1021/jacs.7b12916.

37 S. Dissegna, K. Epp, W. R. Heinz, G. Kieslich and R. A. Fischer, Defective Metal-Organic Frameworks, *Adv. Mater.*, 2018, **30**(37), 1704501, DOI: 10.1002/adma.201704501.

38 S. Naghdi, E. Brown, M. Zendehbad, *et al.*, Glyphosate Adsorption from Water Using Hierarchically Porous Metal–Organic Frameworks, *Adv. Funct. Mater.*, 2023, **33**(20), 2213862, DOI: 10.1002/adfm.202213862.

39 B. Bueken, N. Van Velthoven, A. Krajnc, *et al.*, Tackling the Defect Conundrum in UiO-66: A Mixed-Linker Approach to Engineering Missing Linker Defects, *Chem. Mater.*, 2017, **29**(24), 10478–10486, DOI: 10.1021/acs.chemmater.7b04128.

40 S. Dissegna, K. Epp, W. R. Heinz, G. Kieslich and R. A. Fischer, Defective Metal-Organic Frameworks, *Adv. Mater.*, 2018, **30**(37), 1704501, DOI: 10.1002/adma.201704501.

41 M. Li, X. Liu, Y. Che, *et al.*, Controlled Partial Linker Thermolysis in Metal-Organic Framework UiO-66-NH2 to Give a Single-Site Copper Photocatalyst for the Functionalization of Terminal Alkynes, *Angew. Chem., Int. Ed.*, 2023, **62**(36), e202308651, DOI: 10.1002/anie.202308651.

42 P. Guo, H. Cheng, X. Zeng, *et al.*, Defective Metal-Organic Frameworks with Tunable Porosity and Metal Active Sites for Significantly Improved Performance in Styrene Oxidation, *ChemPlusChem*, 2022, **87**(12), e202200303, DOI: 10.1002/cplu.202200303.

43 R. Huang, Y. Peng, C. Wang, Z. Shi and W. Lin, A Rhenium-Functionalized Metal–Organic Framework as a Single-Site Catalyst for Photochemical Reduction of Carbon Dioxide, *Eur. J. Inorg. Chem.*, 2016, **2016**(27), 4358–4362, DOI: 10.1002/ejic.201600064.

44 J. Hawecker, J. M. Lehn and R. Ziessel, Electrocatalytic reduction of carbon dioxide mediated by Re(bipy)(CO)3Cl (bipy = 2,2′-bipyridine), *J. Chem. Soc., Chem. Commun.*, 1984, (6), 328–330, DOI: 10.1039/C39840000328.

45 M. Taddei, P. V. Dau, S. M. Cohen, *et al.*, Efficient microwave assisted synthesis of metal–organic framework UiO-66: optimization and scale up, *Dalton Trans.*, 2015, **44**(31), 14019–14026, DOI: 10.1039/C5DT01838B.

46 G. C. Shearer, S. Chavan, J. Ethiraj, *et al.*, Tuned to Perfection: Ironing Out the Defects in Metal–Organic Framework UiO-66, *Chem. Mater.*, 2014, **26**(14), 4068–4071, DOI: 10.1021/cm501859p.

47 M. J. Cliffe, W. Wan, X. Zou, *et al.*, Correlated defect nanoregions in a metal–organic framework, *Nat. Commun.*, 2014, **5**(1), 4176, DOI: 10.1038/ncomms5176.

48 G. C. Shearer, S. Chavan, S. Bordiga, S. Svelle, U. Olsbye and K. P. Lillerud, Defect Engineering: Tuning the Porosity and Composition of the Metal–Organic Framework UiO-66 via Modulated Synthesis, *Chem. Mater.*, 2016, **28**(11), 3749–3761, DOI: 10.1021/acs.chemmater.6b00602.

49 M. J. Cliffe, J. A. Hill, C. A. Murray, F. X. Coudert and A. L. Goodwin, Defect-dependent colossal negative thermal expansion in UiO-66(Hf) metal–organic framework, *Phys. Chem. Chem. Phys.*, 2015, **17**(17), 11586–11592, DOI: 10.1039/C5CP01307K.

50 F. Vermoortele, B. Bueken, G. Le Bars, *et al.*, Synthesis Modulation as a Tool To Increase the Catalytic Activity of Metal–Organic Frameworks: The Unique Case of UiO-66(Zr), *J. Am. Chem. Soc.*, 2013, **135**(31), 11465–11468, DOI: 10.1021/ja405078u.

51 M. Thommes, K. Kaneko, A. V. Neimark, *et al.*, Physisorption of gases, with special reference to the evaluation of surface area and pore size distribution (IUPAC Technical Report), *Pure Appl. Chem.*, 2015, **87**(9–10), 1051–1069, DOI: 10.1515/pac-2014-1117.

52 A. R. Hughes and F. Blanc, Recent advances in probing host–guest interactions with solid state nuclear magnetic resonance, *CrystEngComm*, 2021, **23**(13), 2491–2503, DOI: 10.1039/D1CE00168J.

53 H. C. Hoffmann, M. Debowski, P. Müller, *et al.*, Solid-State NMR Spectroscopy of Metal–Organic Framework Compounds (MOFs), *Materials*, 2012, **5**(12), 2537–2572, DOI: 10.3390/ma5122537.

54 M. Waki, Y. K. ichi, S. Shirai, *et al.*, Re(bpy)(CO)3Cl Immobilized on Bipyridine-Periodic Mesoporous Organosilica for Photocatalytic CO2 Reduction, *Chem.–Eur. J.*, 2018, **24**(15), 3846–3853, DOI: 10.1002/chem.201705792.

55 L. A. Faustino, B. L. Souza, B. N. Nunes, *et al.*, Photocatalytic CO2 Reduction by Re(I) Polypyridyl Complexes Immobilized on Niobates Nanoscrolls, *ACS Sustain. Chem. Eng.*, 2018, **6**(5), 6073–6083, DOI: 10.1021/acssuschemeng.7b04713.

56 O. Lanaridi, Y. Chen, J. N. Blaschke, P. Ayala, B. C. Bayer, D. Eder and A. Limbeck, Introducing a modified sample preparation and straightforward elemental ratio determination strategy with LA-ICP-MS to expand the nanoparticle probing toolkit, *Advances in Sample Preparation*, 2025, **16**, 100223, DOI: 10.1016/j.sampre.2025.100223.

57 H. Zou, L. J. Arachchige, W. Rong, *et al.*, Low-Valence Metal Single Atoms on Graphdiyne Promotes Electrochemical Nitrogen Reduction via M-to-N2 π-Backdonation, *Adv. Funct. Mater.*, 2022, **32**(24), 2200333, DOI: 10.1002/adfm.202200333.

58 B. Mennucci, Polarizable continuum model, *WIREs Comput. Mol. Sci.*, 2012, **2**(3), 386–404, DOI: 10.1002/wcms.1086.

59 B. Delley, The conductor-like screening model for polymers and surfaces, *Mol. Simul.*, 2006, **32**(2), 117–123, DOI: 10.1080/08927020600589684.
60 C. Dupont, O. Andreussi and N. Marzari, Self-consistent continuum solvation (SCCS): The case of charged systems, *J. Chem. Phys.*, 2013, **139**(21), 214110, DOI: 10.1063/1.4832475.
61 J. Filser, K. Reuter and H. Oberhofer, Piecewise Multipole-Expansion Implicit Solvation for Arbitrarily Shaped Molecular Solutes, *J. Chem. Theory Comput.*, 2022, **18**(1), 461–478, DOI: 10.1021/acs.jctc.1c00834.
62 J. W. Essex and W. L. Jorgensen, Dielectric constants of formamide and dimethylformamide via computer simulation, *J. Phys. Chem.*, 1995, **99**(51), 17956–17962, DOI: 10.1021/j100051a021.
63 D. Sun, Y. Fu, W. Liu, *et al.*, Studies on Photocatalytic CO2 Reduction over NH2-Uio-66(Zr) and Its Derivatives: Towards a Better Understanding of Photocatalysis on Metal–Organic Frameworks, *Chem.–Eur. J.*, 2013, **19**(42), 14279–14285, DOI: 10.1002/chem.201301728.
64 S. Meister, R. O. Reithmeier, M. Tschurl, U. Heiz and B. Rieger, Unraveling Side Reactions in the Photocatalytic Reduction of CO2: Evidence for Light-Induced Deactivation Processes in Homogeneous Photocatalysis, *ChemCatChem*, 2015, **7**(4), 690–697, DOI: 10.1002/cctc.201402984.

